

CHEMISTRY

Stitching h-BN by atomic layer deposition of LiF as a stable interface for lithium metal anode

Jin Xie,^{1*} Lei Liao,^{1*} Yongji Gong,¹ Yanbin Li,¹ Feifei Shi,¹ Allen Pei,¹ Jie Sun,¹ Rufan Zhang,¹ Biao Kong,¹ Ram Subbaraman,² Jake Christensen,² Yi Cui^{1,3†}

Defects are important features in two-dimensional (2D) materials that have a strong influence on their chemical and physical properties. Through the enhanced chemical reactivity at defect sites (point defects, line defects, etc.), one can selectively functionalize 2D materials via chemical reactions and thereby tune their physical properties. We demonstrate the selective atomic layer deposition of LiF on defect sites of h-BN prepared by chemical vapor deposition. The LiF deposits primarily on the line and point defects of h-BN, thereby creating seams that hold the h-BN crystallites together. The chemically and mechanically stable hybrid LiF/h-BN film successfully suppresses lithium dendrite formation during both the initial electrochemical deposition onto a copper foil and the subsequent cycling. The protected lithium electrodes exhibit good cycling behavior with more than 300 cycles at relatively high coulombic efficiency (>95%) in an additive-free carbonate electrolyte.

INTRODUCTION

h-BN, a two-dimensional (2D) atomic crystal, has emerged as an attractive material for various applications in electronics (1–3) and optoelectronics (4, 5) due to its unique electrical and optical properties. In addition, it has a superior chemical inertness, making it stable against most chemicals such as oxygen (6) and Li metal (7). Perfect single atomic layer of h-BN has very strong mechanical strength with a predicted in-plane Young's modulus approaching 1.0 TPa (8). Because of these advantages, h-BN has shown recent success as a stable coating that prevents metal oxidation at high temperatures (6) and suppresses lithium dendrite formation during electrochemical lithium metal plating (7). Many of the abovementioned applications require large-area and high-quality h-BN. Although chemical vapor deposition (CVD) has emerged as one of the most powerful methods to prepare high-quality h-BN (9–15), CVD h-BN still has numerous defects intrinsic to the synthesis and transfer processes. h-BN prepared by CVD is typically polycrystalline and has a grain size on the order of a few hundred nanometers to a few tens of micrometers with a high density of point defects (12–15). Moreover, the transfer processes of 2D materials also introduce different kinds of defects such as cracks (16–18) and wrinkles (19, 20). These defects serve as a double-edged sword. On the one hand, their existence may compromise the effectiveness of h-BN as a stable interfacial layer in the abovementioned applications. On the other hand, the defects surrounded by dangling bonds provide possible anchoring sites for selective chemical modification to an otherwise chemically inert (arising from the strong B–N bonds) h-BN layer, however, to take place on h-BN. They provide a rich chemistry for us to tune the properties of h-BN.

Previous experimental and theoretical studies have shown enhanced chemical reactivity at the edge (21) and defect sites (22, 23) in graphene, but such a case study of h-BN is still missing in the literature. The chemical functionalization at defect sites may greatly improve the chemical and mechanical stability of h-BN, which is especially important for h-BN when applications such as surface protection are of interest.

For instance, theoretical simulation has shown that grain boundaries present mechanically weakened points, and therefore, single-layer h-BN with small grain sizes has smaller elastic modulus and tensile strength compared to defect-free single-crystalline single-layer h-BN (24). For multilayer and bulk 2D materials, degradation through chemical (25) and electrochemical (26–29) exfoliation has also been observed.

With the highest specific capacity of ~3860 mA-hour/g, Li metal has long been considered to be the most promising candidate anode material to enable the Li-S and Li-O₂ technology, which can in turn offer 5 to 10 times increased overall energy density as compared to Li-ion battery technology (30–34). However, the commercial application of Li metal anodes has been limited by two fundamental challenges. First, Li metal is strongly reducing and tends to react with battery electrolytes to form a solid electrolyte interphase (SEI) (28, 35). The reaction at the electrode/electrolyte interface consumes both active Li and an electrolyte. Second, because of the virtually infinite relative volume change in Li metal anodes, the naturally formed SEI layer is weak against mechanical deformation, and it undergoes continuous formation and breakdown upon battery cycling (32, 34). Together, the chemical and mechanical instability cause dendritic Li plating/stripping with low coulombic efficiencies, which can limit the cycle life of batteries and lead to shorting and potentially severe safety events. The high-surface area Li also enhances the kinetics of thermal abuse reactions, effectively lowering the temperature at which thermal runaway can occur. A few interfacial materials [for example, 2D materials (7, 36, 37), carbon spheres (38), ceramic solid electrolytes (39), fluorides (40, 41), oxides (42), and phosphates (43)] have been investigated. Among them, 2D materials are promising candidates, owing to their high mechanical strength, chemical stability, and flexibility. Previous attempts at using CVD h-BN as an interfacial layer have shown some promise, although the weak bonding at the domain boundaries present issues for maintaining the stable interface over long cycling (7). Here, we demonstrate the selective atomic layer deposition (ALD) of LiF on CVD h-BN and propose its application as a chemically and mechanically stable interfacial layer for stable Li metal cycling. The selective deposition, via ALD, allows us to deposit LiF onto defect sites of CVD h-BN and void space where there is no h-BN coverage. The selectivity was confirmed by atomic force microscopy (AFM), Auger spectroscopy, scanning electron microscopy (SEM), and transmission electron microscopy (TEM). LiF is a key component in an SEI in Li-ion batteries, and it has a wide

¹Department of Materials Science and Engineering, Stanford University, Stanford, CA 94305, USA. ²Bosch Research and Technology Center North America, 4005 Miranda Avenue #200, Palo Alto, CA 94304, USA. ³Stanford Institute for Materials and Energy Sciences, SLAC National Accelerator Laboratory, 2575 Sand Hill Road, Menlo Park, CA 94025, USA.

*These authors contributed equally to this work.

†Corresponding author. Email: yicui@stanford.edu

electrochemical stability window, which makes it stable against Li metal (44). Recently, Lu *et al.* (45) demonstrated that the addition of LiF could improve the stability of Li metal anode during cycling. LiF could also improve the surface diffusion of ions and therefore leads to smooth Li plating (40, 41, 46). Therefore, LiF is an ideal candidate to serve as molecular stitches that hold polycrystalline CVD h-BN domains strongly together using selective ALD. The chemically and mechanically stable hybrid LiF/h-BN film successfully suppressed lithium dendrite formation during initial electrochemical deposition onto a copper foil and during subsequent cycling. The protected lithium electrodes were cycled more than 300 times with a high coulombic efficiency in an additive-free carbonate electrolyte.

RESULTS

Synthesis of ALD LiF and CVD h-BN

Polycrystalline h-BN was prepared in a homebuilt CVD system using heated ammonia borane as the precursor at a growth temperature of 1000°C on Cu foils (see Materials and Methods for more growth details). The morphology and coverage of CVD h-BN on Cu can be carefully controlled by adjusting precursor feeding rates and growth durations. Single-layer h-BN exhibited the typical triangular shape with short growth durations and h-BN triangle domains and then merged to form continuous film with longer growth durations (see the Supplementary Materials). As-grown CVD h-BN was then transferred onto Si substrates with a poly(methyl methacrylate) (PMMA) support for further characterization.

ALD of LiF in this study was carried out using lithium *tert*-butoxide (LiOtBu) and titanium fluoride (TiF₄) as precursors at a growth temperature of 250°C [see Materials and Methods and x-ray photoelectron spectroscopy (XPS) analysis in the Supplementary Materials for more deposition details]. It was performed on various substrates including pristine Si, Cu, and stainless steel (SS). ALD is typically known for its ability to achieve a conformal coating. For instance, the ALD LiF film developed in this study was highly uniform on pristine Si, Cu, and SS substrates with only 50 ALD cycles (see the Supplementary Materials for additional SEM characterization). Conversely, the ALD LiF deposition on h-BN is selective and does not cover the entire substrate. For comparison, h-BN/Si before and after ALD LiF deposition was characterized by SEM (Fig. 1). Although pristine h-BN appears to form complete coverage on Si (Fig. 1B, left), point and line defects cannot be revealed by SEM due to the limitation of resolution. After LiF deposition, there were considerable numbers of nanowires and nanoparticles deposited on the continuous h-BN layer (Fig. 1B, right), indicating the nature of selective ALD LiF deposition on h-BN. The formation of nanowires and nanoparticles might relate to the preferred nucleation of LiF on the line and point defects of CVD h-BN. These phenomena were more obvious at the edge of h-BN; here, LiF nanowires often originated from where two h-BN domains meet. This selective deposition to form LiF nanowires and nanoparticles on h-BN was universal for ALD LiF deposition with different amounts of ALD cycles, from 25 to 150 cycles (see the Supplementary Materials).

Characterization of selective LiF deposition on h-BN

To further analyze the LiF/h-BN hybrid film, we examined morphologies and height profiles of single-layer h-BN with and without ALD LiF deposition by using AFM. To better reveal the selective deposition, we transferred h-BN onto the Si substrate because of its flatness compared to Cu for both SEM and AFM characterizations. The characterization of

surface morphology of selective ALD LiF deposition on h-BN/Cu using SEM was also included in the Supplementary Materials. Single-layer h-BN film was about 1 nm higher than the Si substrate itself (Fig. 2, B and C). After 50 cycles of ALD LiF deposition, the region covered by the h-BN film became lower than the Si substrate without h-BN coverage (Fig. 2, D and F). This discrepancy in height increment observed on Si and h-BN after ALD LiF deposition can be attributed to the different chemical reactivities of Si and h-BN substrates. The native oxide on Si substrate provides rich surface hydroxide functional groups, which can readily react with ALD precursors to initiate the nucleation of LiF. On the contrary, the pristine h-BN film with saturated B–N bonds lacks surface dangling bonds to react with ALD precursors except at defect sites. The nucleation of LiF on the h-BN surface is therefore prohibited, and the average height gain on h-BN was much less than the height gain on Si. In addition to AFM characterization, the uneven nucleation of LiF on Si and h-BN was confirmed using Auger characterization (Fig. 2, G and H). The elemental distribution of boron, nitrogen, and fluorine was mapped. For pristine h-BN on Si, the distribution of boron and nitrogen agreed well with the electron microscopy image. After ALD LiF deposition, the fluorine signal intensified, especially on where there was no initial h-BN coverage. Both AFM and Auger characterizations confirmed the suppressed LiF nucleation on h-BN compared to that on Si.

Nevertheless, we did observe normal height gain on defect sites (highlighted by red arrows in Fig. 2F). CVD h-BN growth is known to start with triangular shape single crystals; however, the formation of grain boundaries with aligned dislocations is inevitable when crystal domains meet with longer growth durations (see the Supplementary Materials). More specifically, two types of dislocations including pentagon-heptagon (“5-7”) and square-octagon (“4-8”) pairs (47, 48) have been theoretically predicted and experimentally observed. The 5-7 pair carries a net positive charge at the B-rich side and negative charge at the N-rich side. It also contains homoelemental bonding (either B–B or N–N), which is less stable than heteroelemental bonding (B–N). Although the 4-8 pair does not contain homoelemental bonding, it has a higher strain energy caused by the distorted rings. The net charge and less stable homoelemental bonding, along with high strain energy, altogether make the h-BN prone to react chemically at the grain boundaries. In addition to the enhanced chemical reactivity at the grain boundaries, point defects such as vacancies in h-BN may serve as anchoring sites for incoming ALD precursors due to the existence of dangling bonds (N–H or B–H) at the edge. Therefore, both nanowires and nanoparticles of LiF were observed in our SEM and AFM characterizations. This selective growth of ALD LiF on h-BN is significant and could, in principle, (i) map out point and line defects in h-BN, (ii) seal pinholes caused by CVD growth and postgrowth transfer, and (iii) improve the overall mechanical properties of the h-BN film.

To further verify the enhanced nucleation at the grain boundaries of h-BN, we used TEM characterization to provide direct evidence. h-BN was suspended on a Au TEM grid with 2- μ m openings using a PMMA-assisted transfer method (see Materials and Methods). After annealing in Ar/H₂ environment at 380°C, the TEM grid with suspended h-BN was subjected to ALD LiF deposition directly. Consistent with SEM characterization, TEM confirmed the scattered LiF nucleation and preferred LiF nucleation along certain lines (highlighted by red arrows). Here, we note that the nucleation density of LiF on suspended h-BN observed in TEM was higher than the nucleation density of LiF on h-BN/Si observed in SEM. This difference might be due to LiF that can nucleate on both sides of suspended h-BN on the TEM grid compared to only one side of h-BN on Si. The nucleation density of ALD LiF particles on

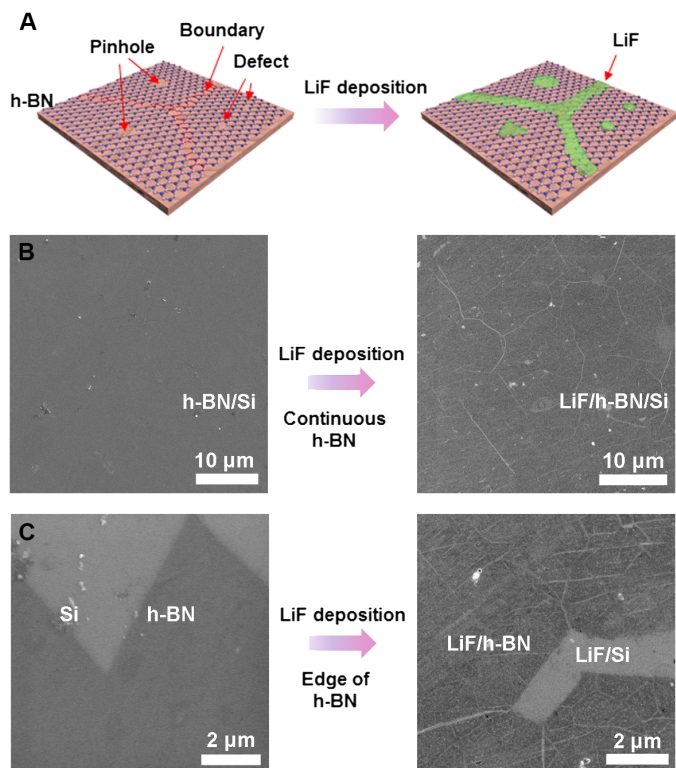


Fig. 1. SEM characterization. (A) Schematics of selective ALD LiF deposition on h-BN. (B) SEM characterization of 50 cycles of ALD LiF deposition on continuous h-BN. (C) SEM characterization of 50 cycles of ALD LiF deposition on the edge of h-BN.

suspended h-BN was ~ 3500 per μm^2 , indicating a high density of point defects. The nucleation density of LiF particles along grain boundaries was two times higher (Fig. 3C). A diffraction pattern was acquired in the blue area where there is a LiF line crossing (Fig. 3B). It showed two sets of h-BN diffraction patterns, which confirms the existence of a grain boundary of CVD h-BN.

With a Gibbs formation energy of -587.7 kJ/mol (49), the thermodynamically stable electrochemical window of LiF is as wide as 0 to 6.1 V versus Li^+/Li . Being a key component in the SEI, LiF is also chemically stable against various reactive species in the battery such as Li metal and HF. Therefore, LiF is a potential candidate to function as a stable interfacial layer. The concern of using LiF as the protection layer lies mainly in its poor Li-ion conductivity. Nevertheless, these problems can be alleviated if an ultrathin layer or a composite layer can be obtained. For composite films containing LiF nanoparticles, enhanced Li-ion conductivity at the interface has been observed (50). Here, ALD provides a way to fine-tune the coating thickness of LiF thin films or the size of LiF nanoparticles to battle the poor ionic conductivity of LiF.

Suppression of dendrite formation during Li plating

We then studied the morphology of Li plating in an additive-free carbonate electrolyte on various substrates using SEM. The Li plated on Cu exhibited the typical dendritic growth (Fig. 4, A to C). The Li whiskers have irregular shapes and a mean diameter in the range of several hundred nanometers. However, we found that the electrochemical plating of Li on ALD LiF/Cu (Fig. 4, G to I) was even less uniform than that on pristine Cu. The plated Li on LiF/Cu did not cover the entire substrate, and it was dendritic in nature. LiF deposited directly on the Cu current

collector poses many challenges for the Li deposition/stripping reactions. First, LiF has poor electrical conductivity, which leads to an increased overpotential. Second, the LiF film deposited by ALD has strong chemical bonding with the underlying Cu foil, which leads to lack of obvious Li nucleation sites. For example, the initial nucleation of Li plating prefers to take place between LiF particles rather than underneath it. Even if some Li managed to deposit underneath the LiF film, it will crack the LiF film because LiF is not mechanically flexible. Once the nucleation occurs, further Li deposition is preferred on the existing nucleation sites rather than forming additional Li nuclei on top of the nonconductive LiF film or underneath the LiF film by breaking the LiF shell. The low nucleation density leads to a high initial plating overpotential and nonuniform plating.

Compared to the nature of strong chemical binding between LiF and Cu, the physical interaction between h-BN and Cu is considerably weaker. For instance, 2D materials such as graphene can be lifted from the substrate via hydrogen generation (51). Our previous results have also shown that h-BN can be lifted by the Li plated underneath (7). However, in spite of a high theoretical in-plane Young's modulus, the grain boundaries are predicted to be the weak points of h-BN when tensile stress is applied (24). Although we started with a continuous CVD h-BN film, holes appeared after Li plating (Fig. 4, D to F). Upon closer inspection, dendritic Li was found to be growing within. These holes can be a result of (i) the broken film at the weak grain boundaries or point defects due to stress induced by Li plating, (ii) pinholes remaining after the CVD growth, and (iii) cracks caused by the transfer process.

Using the LiF/h-BN hybrid film as the interfacial layer combines the advantages of both components. First, the weak physical interaction between h-BN and Cu allows Li to be plated in between h-BN and Cu. Second, with the addition of chemically stable LiF linkers, the overall mechanical strength of LiF/h-BN is improved. It also helps to seal any pinholes or cracks induced in the CVD synthesis and transfer. The superior chemical and mechanical stability of the LiF/h-BN combination effectively suppressed the Li dendrite formation. The resulting electrochemical plating of Li is smooth and uniform (Fig. 4, J to L).

Electrochemical performance

Long-term Li plating/stripping experiments were also conducted on Cu, h-BN/Cu, LiF/Cu, and LiF/h-BN/Cu substrates in EC/DEC electrolyte with 1 M LiPF_6 containing no additives (Fig. 5). Li with a total capacity of 1 mA-hour/ cm^2 was plated on the corresponding working electrode at a rate of 0.5 mA/ cm^2 . The working electrode was then cycled to a cutoff potential of 2.0 V versus Li^+/Li at the same rate of 0.5 mA/ cm^2 to strip the deposited Li. The coulombic efficiency was defined as the Li stripping capacity divided by the Li plating capacity for each cycle. The coulombic efficiencies on the Cu substrate steadily decreased as cycling progressed, dropping to $\sim 70\%$ in 90 cycles, indicating significant side reactions between Li and the electrolyte. The consumption of Li and the electrolyte through side reactions is undesirable for achieving a long-term stable Li metal anode.

Among the three types of modified substrates, LiF/Cu had the poorest cycling performance, which was even worse than pristine Cu. As discussed above, the electrochemical Li plating on LiF/Cu was nonuniform across the substrate. Because of the poor conductivity of LiF and strong adhesion between LiF and Cu, the initial Li nucleation is difficult, leading to a high overpotential although only a few nanometers of LiF was deposited (Fig. 5 B). For comparison, the initial Li nucleation overpotentials on LiF/Cu and Cu substrates in the beginning of the

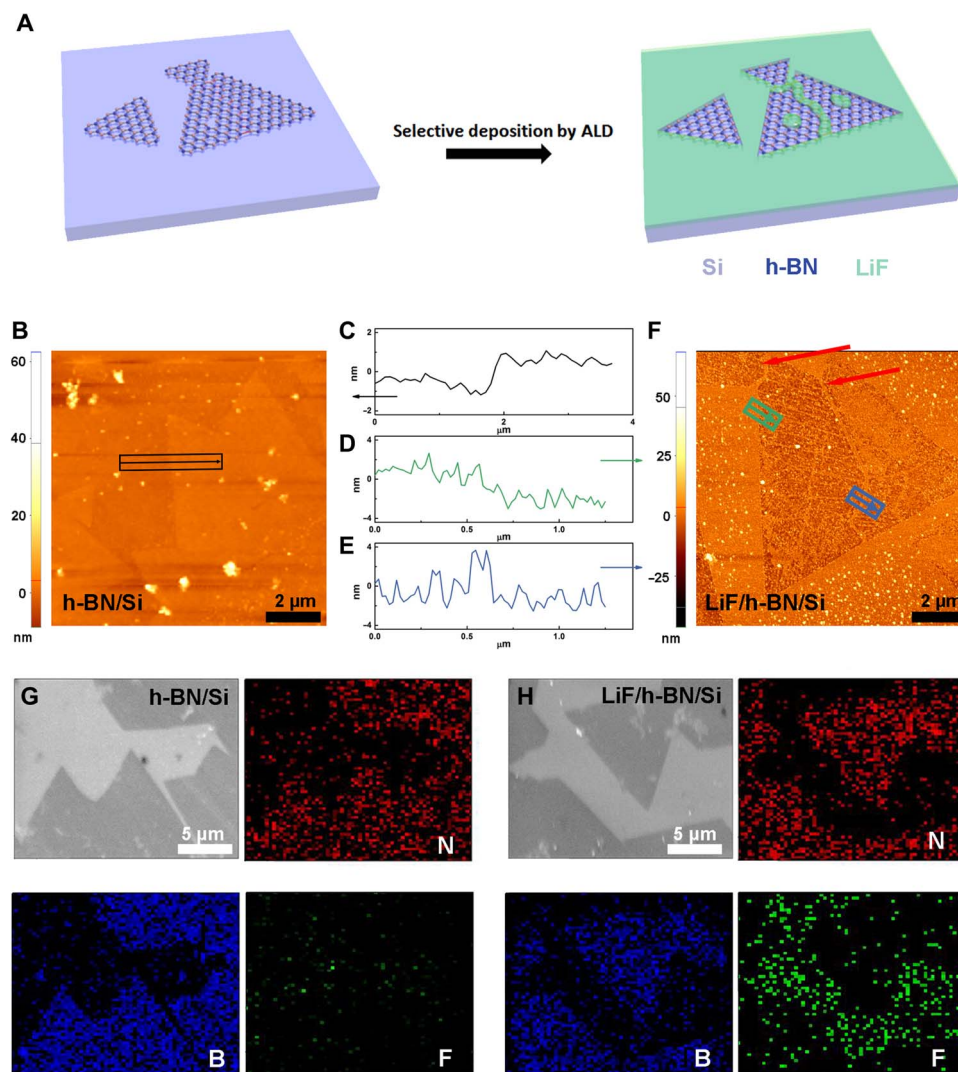


Fig. 2. AFM and Auger characterization. (A) Top-view and side-view schematics of selective ALD LiF deposition on h-BN/Si. (B) AFM characterization of single-layer h-BN on a Si substrate. (C) Height profile of single-layer h-BN on a Si substrate. (D and E) Height profiles of ALD LiF-coated single-layer h-BN on a Si substrate. (F) AFM characterization of ALD LiF-coated single-layer h-BN on a Si substrate. (G) Elemental mapping of N, B, and F using Auger spectroscopy for h-BN/Si. (H) Elemental mapping of N, B, and F using Auger spectroscopy for LiF/h-BN/Si.

second Li plating half-cycle were 164 and 64 mV, respectively. The average Li plating overpotentials on LiF/Cu and Cu substrates throughout the second Li plating half-cycle were 80 and 60 mV, respectively. In addition, the fact that we see coulombic efficiency on the LiF/Cu substrate fluctuating in its late cycles may suggest dead Li formation. Because of the poor electrical conductivity of LiF on Cu, when Li dendrites lose the physical connection to the underlying Li base, it is difficult to reestablish their electrical connection to the substrate because a good portion of the substrate was covered with poorly conductive LiF. This part of disconnected Li then becomes dead Li, and we observe a low coulombic efficiency (cycle 46 in Fig. 5C). In the following cycles, if dead Li reestablishes an electrical connection to the underlying Li by chance, then we can observe a coulombic efficiency higher than 100% (cycle 54 in Fig. 5D). Collectively, cells using LiF/Cu as the current collector suffered from a low Li nucleation density, high overpotential, and poor plating uniformity, all contributing to their poor cycle performance.

In contrast, Li plating/stripping on h-BN/Cu was considerably more stable than that on pristine Cu with both lower overpotentials and higher coulombic efficiencies over long cycles. At the second cycle, the initial nucleation barrier on h-BN/Cu was only 64 mV, and the average Li plating overpotential was only 42 mV. The average coulombic efficiency during the first 100 cycles was 92.2%, which then dropped to ~70% after ~150 total cycles. As plating/stripping cycles progressed, the h-BN layer may have slowly broken apart starting from defective sites and became exfoliated from the substrate, eventually losing its ability to minimize the side reactions between Li and the electrolyte.

Most excitingly, LiF/h-BN/Cu stood out among the three types of modified substrates in the long-term cycle stability test. Benefiting from the weak interaction between h-BN and Cu, the Li plating readily took place underneath LiF/h-BN. At the second cycle, the initial nucleation barrier on LiF/h-BN/Cu was only 60 mV, and the average Li plating overpotential was only 47 mV (Fig. 5B). The overpotential for Li plating

on LiF/h-BN/Cu was not significantly higher than that on pristine Cu. This low overpotential was benefited from three aspects. First, LiF prepared by ALD is ultrathin on h-BN, which could offset its low Li-ion conductivity. In addition, LiF improves the surface diffusion of ions, and simulations have shown reduced Li-ion diffusion energy barrier for LiF-enriched SEI (40, 41). Second, the Li-ion diffusion energy barriers are much lower at the defects of 2D materials (37). Although a perfect defect-free h-BN would have high mechanical strength, it will be difficult for Li ion to diffuse through. Here, by coating LiF on defect sites

of h-BN, we can improve the stability of h-BN while still allowing Li ion to diffuse through. Third, LiF/h-BN interfacial layer minimizes the parasitic chemical reactions between the Li metal and the liquid electrolyte. After 90 cycles, the average Li plating/stripping overpotential on LiF/h-BN/Cu was lower than that on pristine Cu (Fig. 5E), indicating less SEI buildup. The Li plating/stripping on the LiF/h-BN/Cu substrate maintained a high average coulombic efficiency above 96% for over 300 cycles in the carbonate electrolyte without the aid of any electrolyte additives. The significantly improved coulombic efficiency suggests that the LiF/h-BN is effective in protecting Li from reacting with the electrolyte. The coulombic efficiency versus cycle number curve was also the smoothest one among the four types of substrates, suggesting a low degree of dead Li formation and detachment on LiF/h-BN/Cu. In addition, the cycle performance of electrodes with different protection films was tested in EC/DEC electrolyte with 1% vinylene carbonate and 10% fluoroethylene carbonate as additives (see the Supplementary Materials). The coulombic efficiencies and cycle lives of different electrodes can be further improved to different degrees by additives (see the Supplementary Materials for a detailed discussion). A similar approach of combining additives and 2D materials was also reported by Kim *et al.* (36). To summarize, the good cycle stability on LiF/h-BN/Cu resulted from (i) the low binding affinity between h-BN and Cu so that LiF/h-BN can be lifted by Li plated underneath, (ii) strong mechanical and stable chemical properties of the LiF/h-BN hybrid film, and (iii) reduced side reactions between plated Li and the electrolyte.

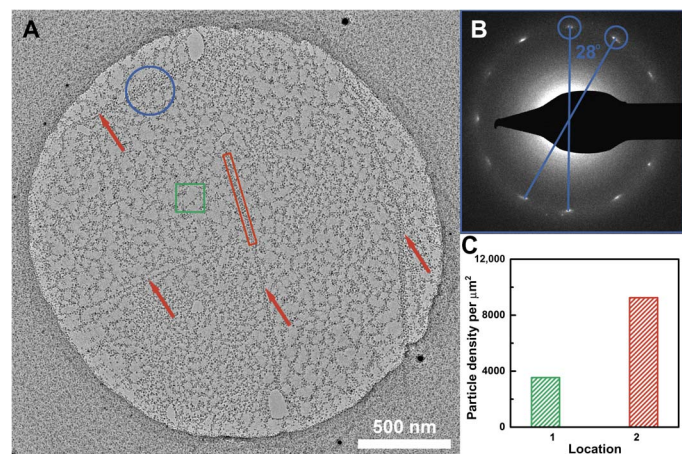


Fig. 3. TEM characterization. (A) TEM characterization of ALD LiF deposition on suspended h-BN. (B) Diffraction pattern of the highlighted blue area. (C) Comparison of particle densities of the highlighted green and red areas.

Cross section of cycled electrodes

To further analyze the Li deposition morphology, we acquired cross-section SEM images after repeated plating/stripping cycles. Focused

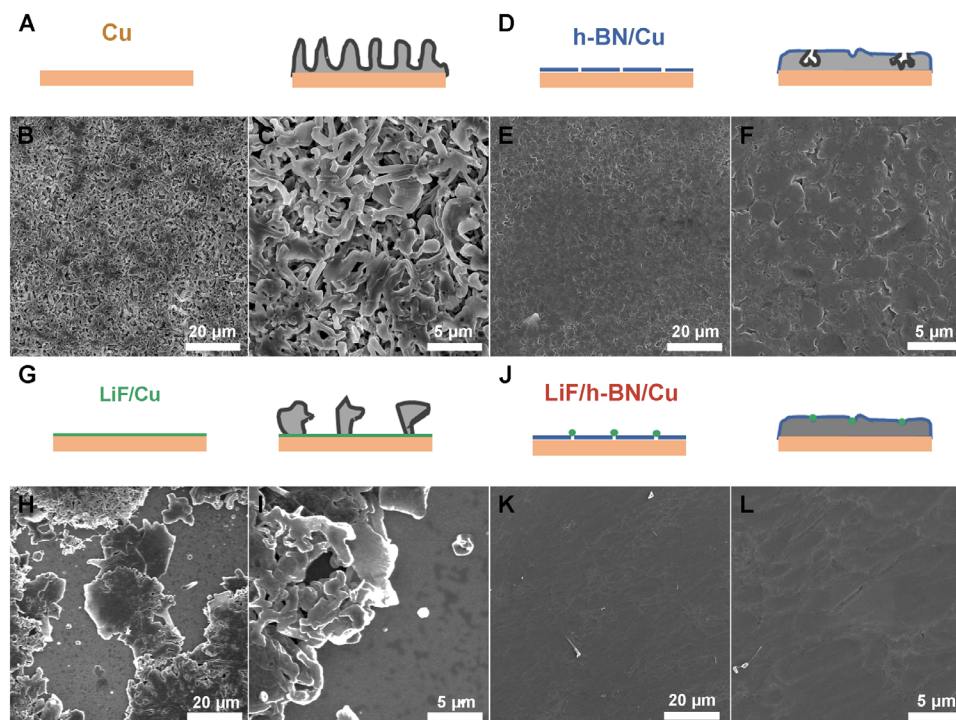


Fig. 4. SEM characterization of electrochemically plated Li. Schematics and SEM characterization of Li plating on Cu (A to C), h-BN/Cu (D to F), LiF/Cu (G to I), and LiF/h-BN/Cu (J to L). Li plating was performed at a rate of 0.5 mA/cm² and a total capacity of 1 mA-hour/cm² in ethylene carbonate (EC)/diethyl carbonate (DEC) electrolyte with 1 M LiPF₆.

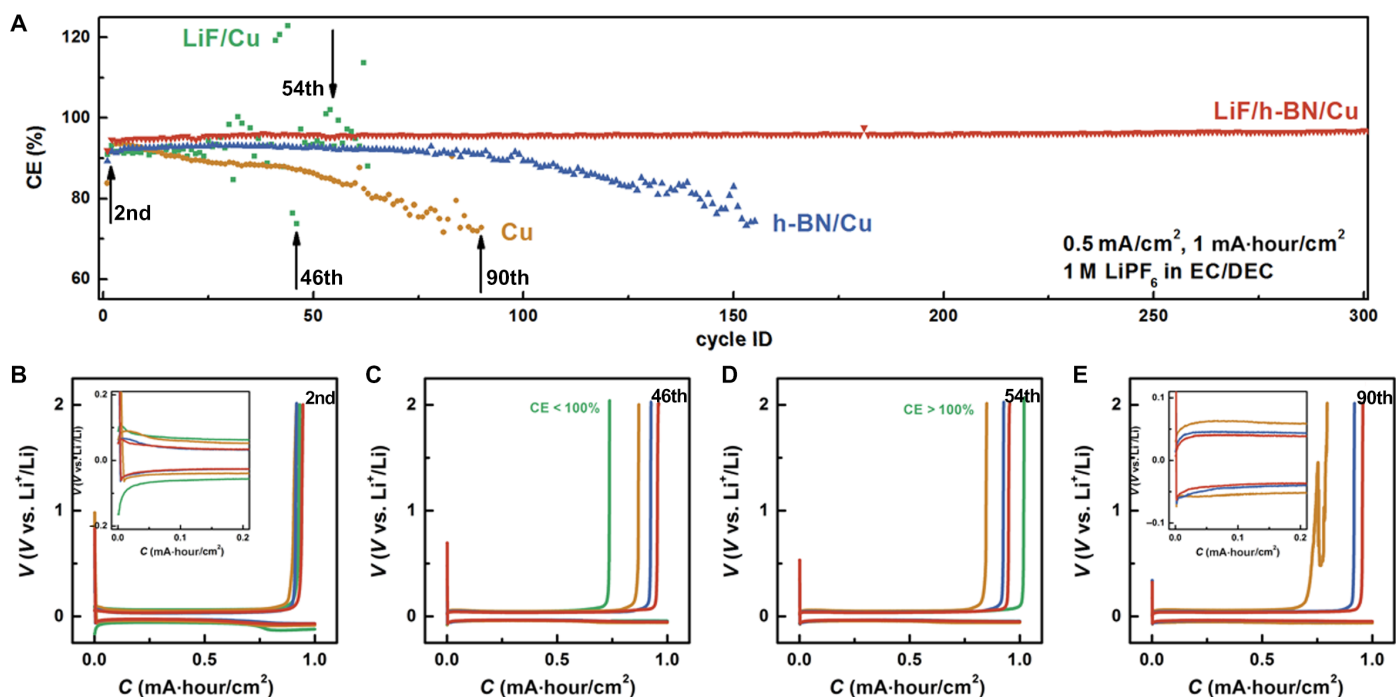


Fig. 5. Cycling performance of repeated Li plating/stripping on Cu, h-BN/Cu, LiF/Cu, and LiF/h-BN/Cu substrates in EC/DEC electrolyte containing 1 M LiPF₆. (A) Coulombic efficiency (CE) versus cycle number plots. (B) Voltage versus capacity plot during second cycle. (C) Voltage versus capacity plot during the 46th cycle. (D) Voltage versus capacity plot during the 54th cycle. (E) Voltage versus capacity plot during the 90th cycle.

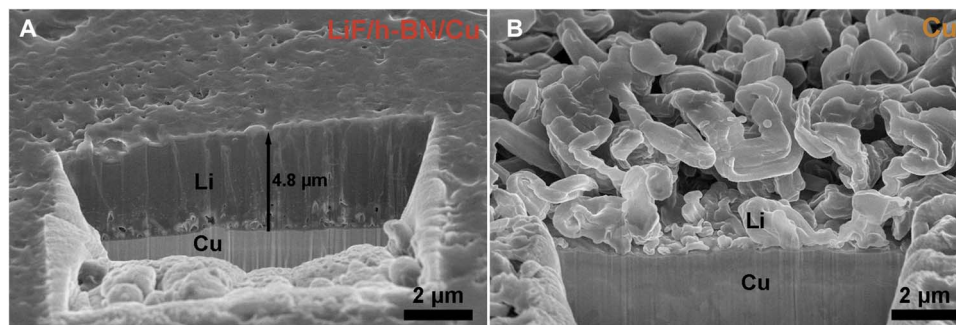


Fig. 6. SEM characterization of cross-section morphologies of electrochemically plated Li. SEM characterization of cross-section morphologies of Li deposited on LiF/h-BN/Cu (A) and pristine Cu (B) substrates after five cycles in EC/DEC electrolyte with 1 M LiPF₆. SEM images were taken with a sample rotation angle of 52°.

ion beam (FIB) was applied to cut fresh plated Li to better reveal the Li deposition morphology underneath the surface coating layer. Li plated on the LiF/h-BN/Cu substrate was not only smoother on the surface but also packed more densely underneath the surface compared to Li plated on pristine Cu. Although there were still few void spaces at the interface between Li and Cu on the LiF/h-BN/Cu substrate, they were possibly caused by the nucleation of Li on Cu substrate. Individual Li grains then grew in size and merged eventually. The average thickness of Li plated on LiF/h-BN/Cu is 4.8 μm (Fig. 6A), which is close to the theoretical thickness (4.85 μm) of dense Li (0.534 g/cm³) with a total capacity of 1 mA-hour/cm². However, it was difficult to identify the exact position of LiF/h-BN after Li plating. XPS analysis (see the Supplementary Materials) shown an SEI formed by the electrochemical reduction of electrolyte covered on the surface of LiF/h-BN. Nevertheless, the LiF/h-BN film remained chemically and mechanically intact, which could

prevent electrochemically plated Li from reacting with air in the ambient environment (see the Supplementary Materials). On the contrary, the Li morphology remained dendritic on the surface of pristine Cu. Underneath the surface, void spaces were visible everywhere across different depths of plated Li. This dendritic Li with a high surface area is undesired for long-term cycling. The continuous formation and cracking of ineffective SEI upon Li volume change during plating/stripping would consume both active Li and the electrolyte. This also explains the low coulombic efficiency we have observed on pristine Cu electrode. Because Li is in excess in the counter electrode, the depletion of electrolyte was likely the cause for the battery failure (see the Supplementary Materials). In comparison, with a stable LiF/h-BN hybrid film as an artificial SEI with strong mechanical property and stable chemical stability, we expect that the side reactions between Li and the electrolyte were minimized and that the battery cycle life can be greatly extended.

DISCUSSION

To summarize, we demonstrated the selective ALD of LiF at defect sites of h-BN with enhanced chemical reactivities. The selective deposition allows us to visualize the location of defects in h-BN using SEM, AFM, and TEM. The chemically and electrochemically stable LiF served as ideal molecular stitches to seal the polycrystalline CVD h-BN. With its superior chemical and mechanical properties, the LiF/h-BN hybrid film effectively suppressed Li dendrite formation and improved the coulombic efficiency of Li metal cycling during long cycles.

MATERIALS AND METHODS

Materials synthesis and preparation

ALD LiF deposition was performed on different types of substrates including Si, SS, Cu, BN/Si, and BN/Cu using a Savannah S100 ALD system (Cambridge NanoTech) (44). The deposition consists of alternating pulse and purge of LiOtBu (97%, Sigma-Aldrich) and TiF₄ (Sigma-Aldrich) as precursors. TiF₄ was gently grinded in an Ar glove box before using. The typical pulse and purge durations for LiOtBu sub-cycle are 1 and 25 s, respectively. The typical pulse and purge durations for TiF₄ sub-cycle are 0.1 and 25 s, respectively. LiOtBu was heated to 160 to 170°C, and TiF₄ was kept at 115 to 125°C. High-purity Ar was used as the carrier gas and purging gas. LiF thin films were obtained at a deposition temperature of 250°C.

h-BN was synthesized in a homebuilt CVD system. Before the deposition, the Cu foil (99.8%, Alfa Aesar) was electrochemically polished by holding 1.5 V versus Cu counter electrode for 60 min in a mixture of phosphoric acid [70 weight % (wt %)] and ethylene glycol (30 wt %) electrolyte. After rinsing and blow-drying, the Cu foil was annealed under 35-standard cubic centimeter per minute (SCCM) H₂ and 50-SCCM Ar flow for 30 min at 1000°C. For the growth of h-BN, 50 mg of ammonia borane (H₃N-BH₃; 97%, Sigma-Aldrich) precursor was loaded into a glass tube attached to the deposition chamber. The precursor vapor was delivered to the deposition chamber when heated by a heating tape wrapped around the glass tube. The h-BN growth was carried out at 1000°C under 35-SCCM H₂ and 50-SCCM Ar flow.

h-BN was transferred to various substrates including Si, SiO₂-coated Si, Cu, and the TEM grid (2- μ m hole size; Ted Pella) with PMMA support. A PMMA solution was spin-coated on the surface of the as-grown h-BN/Cu at speeds of 500 rpm for 60 s, and then 4000 rpm for 30 s. The backside of the Cu foil was cleaned using O₂ plasma and gently wiped with an isopropyl alcohol (IPA)-soaked cotton stick. The sample was then placed into a solution of iron chloride to etch the underlying Cu foil. The PMMA/h-BN films were rinsed with a diluted hydrochloric acid solution and deionized water for three times each. The PMMA/h-BN films were picked up by desired substrates and dried at 60°C. PMMA was removed by soaking in acetone and then in IPA. Finally, samples were annealed in 10-SCCM H₂ and 40-SCCM Ar flow at 380°C for 2 hours to remove residual PMMA to obtain a cleaner h-BN surface.

Material characterizations

AFM was performed using Park XE-70 system with ACTA tips. SEM images of LiF, h-BN, and LiF/h-BN on various substrates were captured in an FEI XL30 Sirion SEM. A Woollam M-2000 Spectroscopic Ellipsometer was used for measuring and fitting optical properties and thicknesses of ALD LiF films on Si substrates. TEM characterization was performed at 80 kV using an FEI Titan. After Li plating/stripping cycling, samples were rinsed in 1,3-dioxolane to remove residual electrolyte and salt for SEM imaging. The morphology of plated Li was ob-

served with an FIB (Nova 600i Dual Beam, FEI). The cycled electrodes were cross-sectioned with a Ga⁺ ion beam and observed with the SEM (JSM-6700F, JEOL). XPS was performed on PHI 5000 VersaProbe using an Al K α ($\lambda = 0.83$ nm and $h\nu = 1486.7$ eV) x-ray source operated at 2 kV and 20 mA.

Electrochemical measurements

Battery cycling performance was evaluated by the galvanostatic cycling of coin cells (CR 2032) with Cu, LiF/Cu, h-BN/Cu, and Li/h-BN/Cu as working electrodes and Li foils (Alfa Aesar) as counter electrodes. The working and counter electrodes were cut into round disks with a diameter of 1 cm and separated by two layers of Celgard separators. Thirty microliters of 1 M LiPF₆ solution in 1:1 (v/v) EC and DEC (BASF) was added as the electrolyte. No additional additive was added into the electrolyte. Battery cycling data were collected using a LAND eight-channel battery tester at room temperature. After assembly, coin cells were galvanostatically cycled between 0 and 2 V at 50 μ A/cm² for five cycles. Battery cycling was then performed by controlling an areal capacity of 1 mA-hour/cm² for Li plating and a cutoff potential of 2 V versus Li⁺/Li for Li stripping during each cycle. The coulombic efficiency was defined as the Li stripping capacity divided by the Li plating capacity.

SUPPLEMENTARY MATERIALS

Supplementary material for this article is available at <http://advances.sciencemag.org/cgi/content/full/3/11/eaa03170/DC1>

fig. S1. SEM characterization of CVD h-BN.

fig. S2. SEM characterization of ALD LiF on Si.

fig. S3. SEM characterization of ALD LiF on h-BN/Si.

fig. S4. SEM characterization of ALD LiF on h-BN/Cu.

fig. S5. SEM characterization of ALD LiF on SS and Cu.

fig. S6. XPS analysis of ALD LiF on Si.

fig. S7. XPS analysis of ALD LiF on h-BN/Cu.

fig. S8. Cycling performance of Cu, h-BN/Cu, and LiF/h-BN/Cu electrodes in carbonate electrolyte with additives.

fig. S9. Optical images of Li-plated Cu, LiF/Cu, h-BN/Cu, and LiF/h-BN/Cu electrodes with different exposure times in the ambient environment.

fig. S10. XPS analysis of the LiF/h-BN/Cu electrode after Li plating.

fig. S11. Cycling performance of batteries with different amounts of electrolyte and failed battery with refilled electrolyte.

References (52–56)

REFERENCES AND NOTES

1. G. R. Dean, A. F. Young, I. Meric, C. Lee, L. Wang, S. Sorgenfrei, K. Watanabe, T. Taniguchi, P. Kim, K. L. Shepard, J. Hone, Boron nitride substrates for high-quality graphene electronics. *Nat. Nanotechnol.* **5**, 722–726 (2010).
2. R. Decker, Y. Wang, V. W. Brar, W. Regan, H.-Z. Tsai, Q. Wu, W. Gannett, A. Zettl, M. F. Crommie, Local electronic properties of graphene on a BN substrate via scanning tunneling microscopy. *Nano Lett.* **11**, 2291–2295 (2011).
3. J. Xue, J. Sanchez-Yamagishi, D. Bulmash, P. Jacquod, A. Deshpande, K. Watanabe, T. Taniguchi, P. Jarillo-Herrero, B. J. LeRoy, Scanning tunnelling microscopy and spectroscopy of ultra-flat graphene on hexagonal boron nitride. *Nat. Mater.* **10**, 282–285 (2011).
4. K. Watanabe, T. Taniguchi, H. Kanda, Direct-bandgap properties and evidence for ultraviolet lasing of hexagonal boron nitride single crystal. *Nat. Mater.* **3**, 404–409 (2004).
5. G.-H. Lee, Y.-J. Yu, X. Cui, N. Petrone, C.-H. Lee, M. S. Choi, D.-Y. Lee, C. Lee, W. J. Yoo, K. Watanabe, T. Taniguchi, C. Nuckolls, P. Kim, J. Hone, Flexible and transparent MoS₂ field-effect transistors on hexagonal boron nitride-graphene heterostructures. *ACS Nano* **7**, 7931–7936 (2013).
6. Z. Liu, Y. Gong, W. Zhou, L. Ma, J. Yu, J. C. Idrobo, J. Jung, A. H. MacDonald, R. Vajtai, J. Lou, P. M. Ajayan, Ultrathin high-temperature oxidation-resistant coatings of hexagonal boron nitride. *Nat. Commun.* **4**, 2541 (2013).

7. K. Yan, H.-W. Lee, T. Gao, G. Zheng, H. Yao, H. Wang, Z. Lu, Y. Zhou, Z. Liang, Z. Liu, S. Chu, Y. Cui, Ultrathin two-dimensional atomic crystals as stable interfacial layer for improvement of lithium metal anode. *Nano Lett.* **14**, 6016–6022 (2014).
8. K. N. Kudin, G. E. Scuseria, B. I. Yakobson, C₂F, BN, and C nanoshell elasticity from ab initio computations. *Phys. Rev. B* **64**, 235406 (2001).
9. Y. Shi, C. Hamsen, X. Jia, K. K. Kim, A. Reina, M. Hofmann, A. L. Hsu, K. Zhang, H. Li, Z.-Y. Juang, M. S. Dresselhaus, L.-J. Li, J. Kong, Synthesis of few-layer hexagonal boron nitride thin film by chemical vapor deposition. *Nano Lett.* **10**, 4134–4139 (2010).
10. L. Song, L. Ci, H. Lu, P. B. Sorokin, C. Jin, J. Ni, A. G. Kvashnin, D. G. Kvashnin, J. Lou, B. I. Yakobson, P. M. Ajayan, Large scale growth and characterization of atomic hexagonal boron nitride layers. *Nano Lett.* **10**, 3209–3215 (2010).
11. K. K. Kim, A. Hsu, X. Jia, S. M. Kim, Y. Shi, M. Dresselhaus, T. Palacios, J. Kong, Synthesis and characterization of hexagonal boron nitride film as a dielectric layer for graphene devices. *ACS Nano* **6**, 8583–8590 (2012).
12. K. K. Kim, A. Hsu, X. Jia, S. M. Kim, Y. Shi, M. Hofmann, D. Nezich, J. F. Rodriguez-Nieva, M. Dresselhaus, T. Palacios, J. Kong, Synthesis of monolayer hexagonal boron nitride on Cu foil using chemical vapor deposition. *Nano Lett.* **12**, 161–166 (2012).
13. L. Wang, B. Wu, J. Chen, H. Liu, P. Hu, Y. Liu, Monolayer hexagonal boron nitride films with large domain size and clean interface for enhancing the mobility of graphene-based field-effect transistors. *Adv. Mater.* **26**, 1559–1564 (2014).
14. X. Song, J. Gao, Y. Nie, T. Gao, J. Sun, D. Ma, Q. Li, Y. Chen, C. Jin, A. Bachmatiuk, M. H. Rummeli, F. Ding, Y. Zhang, Z. Liu, Chemical vapor deposition growth of large-scale hexagonal boron nitride with controllable orientation. *Nano Res.* **8**, 3164–3176 (2015).
15. S. Caneva, R. S. Weatherup, B. C. Bayer, R. Blume, A. Cabrero-Vilata, P. Braeuninger-Weimer, M.-B. Martin, R. Wang, C. Baetz, R. Schloegl, J. C. Meyer, S. Hofmann, Controlling catalyst bulk reservoir effects for monolayer hexagonal boron nitride CVD. *Nano Lett.* **16**, 1250–1261 (2016).
16. X. Li, Y. Zhu, W. Cai, M. Borysiak, B. Han, D. Chen, R. D. Piner, L. Colombo, R. S. Ruoff, Transfer of large-area graphene films for high-performance transparent conductive electrodes. *Nano Lett.* **9**, 4359–4363 (2009).
17. X. Liang, B. A. Sperling, I. Calizo, G. Cheng, C. A. Hacker, Q. Zhang, Y. Obeng, K. Yan, H. Peng, Q. Li, X. Zhu, H. Yuan, A. R. H. Walker, Z. Liu, L.-M. Peng, C. A. Richter, Toward clean and crackless transfer of graphene. *ACS Nano* **5**, 9144–9153 (2011).
18. K. Kim, V. I. Artyukhov, W. Regan, Y. Liu, M. F. Crommie, B. I. Yakobson, A. Zettl, Ripping graphene: Preferred directions. *Nano Lett.* **12**, 293–297 (2012).
19. S. J. Chae, F. Güneş, K. K. Kim, E. S. Kim, G. H. Han, S. M. Kim, H.-J. Shin, S.-M. Yoon, J.-Y. Choi, M. H. Park, C. W. Yang, D. Pribat, Y. H. Lee, Synthesis of large-area graphene layers on poly-nickel substrate by chemical vapor deposition: Wrinkle formation. *Adv. Mater.* **21**, 2328–2333 (2009).
20. Y. Zhang, T. Gao, Y. Gao, S. Xie, Q. Ji, K. Yan, H. Peng, Z. Liu, Defect-like structures of graphene on copper foils for strain relief investigated by high-resolution scanning tunneling microscopy. *ACS Nano* **5**, 4014–4022 (2011).
21. X. Wang, S. M. Tabakman, H. Dai, Atomic layer deposition of metal oxides on pristine and functionalized graphene. *J. Am. Chem. Soc.* **130**, 8152–8153 (2008).
22. K. Kim, H.-B.-R. Lee, R. W. Johnson, J. T. Tanskanen, N. Liu, M.-G. Kim, C. Pang, C. Ahn, S. F. Bent, Z. N. Bao, Selective metal deposition at graphene line defects by atomic layer deposition. *Nat. Commun.* **5**, 4781 (2014).
23. S. Malola, H. Häkkinen, P. Koskinen, Structural, chemical, and dynamical trends in graphene grain boundaries. *Phys. Rev. B* **81**, 165447 (2010).
24. B. Mortazavi, G. Cuniberti, Mechanical properties of polycrystalline boron-nitride nanosheets. *RSC Adv.* **4**, 19137–19143 (2014).
25. W.-Q. Han, L. Wu, Y. Zhu, K. Watanabe, T. Taniguchi, Structure of chemically derived mono- and few-atomic-layer boron nitride sheets. *Appl. Phys. Lett.* **93**, 223103 (2008).
26. S.-K. Jeong, M. Inaba, Y. Iriyama, T. Abe, Z. Ogumi, Surface film formation on a graphite negative electrode in lithium-ion batteries: AFM study on the effects of co-solvents in ethylene carbonate-based solutions. *Electrochim. Acta* **47**, 1975–1982 (2002).
27. Z. Zeng, T. Sun, J. Zhu, X. Huang, Z. Yin, G. Lu, Z. Fan, Q. Yan, H. H. Hng, H. Zhang, An effective method for the fabrication of few-layer-thick inorganic nanosheets. *Angew. Chem. Int. Ed.* **51**, 9052–9056 (2012).
28. D. Aurbach, E. Zinigrad, Y. Cohen, H. Teller, A short review of failure mechanisms of lithium metal and lithiated graphite anodes in liquid electrolyte solutions. *Solid State Ion.* **148**, 405–416 (2002).
29. F. Ding, W. Xu, D. Choi, W. Wang, X. Li, M. H. Engelhard, X. Chen, Z. Yang, J.-G. Zhang, Enhanced performance of graphite anode materials by AlF₃ coating for lithium-ion batteries. *J. Mater. Chem.* **22**, 12745–12751 (2012).
30. P. G. Bruce, S. A. Freunberger, L. J. Hardwick, J.-M. Tarascon, Li–O₂ and Li–S batteries with high energy storage. *Nat. Mater.* **11**, 19–29 (2012).
31. J. Lu, L. Li, J.-B. Park, Y.-K. Sun, F. Wu, K. Amine, Aprotic and aqueous Li–O₂ batteries. *Chem. Rev.* **114**, 5611–5640 (2014).
32. W. Xu, J. Wang, F. Ding, X. Chen, E. Nasybutin, Y. Zhang, J.-G. Zhang, Lithium metal anodes for rechargeable batteries. *Energy Environ. Sci.* **7**, 513–537 (2014).
33. Y. Sun, N. Liu, Y. Cui, Promises and challenges of nanomaterials for lithium-based rechargeable batteries. *Nat. Energy* **1**, 16071 (2016).
34. D. Lin, Y. Liu, Y. Cui, Reviving the lithium metal anode for high-energy batteries. *Nat. Nanotechnol.* **12**, 194–206 (2017).
35. D. Aurbach, E. Zinigrad, H. Teller, P. Dan, Factors which limit the cycle life of rechargeable lithium (metal) batteries. *J. Electrochem. Soc.* **147**, 1274–1279 (2000).
36. J.-S. Kim, D. W. Kim, H. T. Jung, J. W. Choi, Controlled lithium dendrite growth by a synergistic effect of multilayered graphene coating and an electrolyte additive. *Chem. Mater.* **27**, 2780–2787 (2015).
37. H. Tian, Z. W. Seh, K. Yan, Z. Fu, P. Tang, Y. Lu, R. Zhang, D. Legut, Y. Cui, Q. Zhang, Theoretical investigation of 2D layered materials as protective films for lithium and sodium metal anodes. *Adv. Energy Mater.* **7**, 1602528 (2017).
38. G. Zheng, S. W. Lee, Z. Liang, H.-W. Lee, K. Yan, H. Yao, H. Wang, W. Li, S. Chu, Y. Cui, Interconnected hollow carbon nanospheres for stable lithium metal anodes. *Nat. Nanotechnol.* **9**, 618–623 (2014).
39. K. Fu, Y. Gong, B. Liu, Y. Zhu, S. Xu, Y. Yao, W. Luo, C. Wang, S. D. Lacey, J. Dai, Y. Chen, Y. Mo, E. Wachsman, L. Hu, Toward garnet electrolyte-based Li metal batteries: An ultrathin, highly effective, artificial solid-state electrolyte/metallic Li interface. *Sci. Adv.* **3**, e1601659 (2017).
40. S. Choudhury, L. A. Archer, Lithium fluoride additives for stable cycling of lithium batteries at high current densities. *Adv. Electron. Mater.* **2**, 1500246 (2016).
41. L. Fan, H. L. Zhuang, L. Gao, Y. Lu, L. A. Archer, Regulating Li deposition at artificial solid electrolyte interphases. *J. Mater. Chem. A* **5**, 3483–3492 (2017).
42. Y. Zhang, B. Liu, E. Hitz, W. Luo, Y. Yao, Y. Li, J. Dai, C. Chen, Y. Wang, C. Yang, H. Li, L. Hu, A carbon-based 3D current collector with surface protection for Li metal anode. *Nano Res.* **10**, 1356–1365 (2017).
43. N.-W. Li, Y.-X. Yin, C.-P. Yang, Y.-G. Guo, An artificial solid electrolyte interphase layer for stable lithium metal anodes. *Adv. Mater.* **28**, 1853–1858 (2016).
44. J. Xie, A. D. Sendek, E. D. Cubuk, X. Zhang, Z. Lu, Y. Gong, T. Wu, F. Shi, W. Liu, E. J. Reed, Y. Cui, Atomic layer deposition of stable LiAlF₄ lithium ion conductive interfacial layer for stable cathode cycling. *ACS Nano* **11**, 7019–7027 (2017).
45. Y. Lu, Z. Tu, L. A. Archer, Stable lithium electrodeposition in liquid and nanoporous solid electrolytes. *Nat. Mater.* **13**, 961–969 (2014).
46. Y. Yang, Z. Wang, R. Zhou, H. Guo, X. Li, Effects of lithium fluoride coating on the performance of nano-silicon as anode material for lithium-ion batteries. *Mater. Lett.* **184**, 65–68 (2016).
47. A. L. Gibb, N. Alem, J.-H. Chen, K. J. Erickson, J. Ciston, A. Gautam, M. Linck, A. Zettl, Atomic resolution imaging of grain boundary defects in monolayer chemical vapor deposition-grown hexagonal boron nitride. *J. Am. Chem. Soc.* **135**, 6758–6761 (2013).
48. Y. Liu, X. Zou, B. I. Yakobson, Dislocations and grain boundaries in two-dimensional boron nitride. *ACS Nano* **6**, 7053–7058 (2012).
49. J. A. Dean, *Lange's Handbook of Chemistry* (McGraw-Hill, ed. 15, 1998).
50. C. Li, L. Gu, J. Maier, Enhancement of the Li conductivity in LiF by introducing glass/crystal interfaces. *Adv. Funct. Mater.* **22**, 1145–1149 (2012).
51. L. Gao, W. Ren, H. Xu, L. Jin, Z. Wang, T. Ma, L.-P. Ma, Z. Zhang, Q. Fu, L.-M. Peng, X. Bao, H.-M. Cheng, Repeated growth and bubbling transfer of graphene with millimetre-size single-crystal grains using platinum. *Nat. Commun.* **3**, 699 (2012).
52. A. Ibrahim, S. Akhtar, M. Atieh, R. Karnik, T. Laoui, Effects of annealing on copper substrate surface morphology and graphene growth by chemical vapor deposition. *Carbon* **94**, 369–377 (2015).
53. T. Pilvi, K. Arstila, M. Leskelä, M. Ritala, Novel ALD process for depositing CaF₂ thin films. *Chem. Mater.* **19**, 3387–3392 (2007).
54. T. Pilvi, E. Puukilainen, K. Arstila, M. Leskelä, M. Ritala, Atomic layer deposition of LaF₃ thin films using La(thd)₃ and TiF₄ as precursors. *Chem. Vap. Deposition* **14**, 85–91 (2008).
55. X.-Q. Zhang, X.-B. Cheng, X. Chen, C. Yan, Q. Zhang, Fluoroethylene carbonate additives to render uniform Li deposits in lithium metal batteries. *Adv. Funct. Mater.* **27**, 1605989 (2017).
56. F. Ding, W. Xu, X. Chen, J. Zhang, M. H. Engelhard, Y. Zhang, B. R. Johnson, J. V. Crum, T. A. Blake, X. Liu, J.-G. Zhang, Effects of carbonate solvents and lithium salts on morphology and coulombic efficiency of lithium electrode. *J. Electrochem. Soc.* **160**, A1894–A1901 (2013).

Acknowledgments

Funding: Part of this work was performed at the Stanford Nano Shared Facilities and Stanford Nanofabrication Facility. This work was sponsored in part by Robert Bosch LLC through Bosch Energy Research Network grant no. 03.25.SS.15. This work was partially supported by the Assistant Secretary for Energy Efficiency and Renewable Energy, Office of Vehicle Technologies of the U.S. Department of Energy under the Battery Materials Research program and the Battery500 Consortium program. **Author contributions:** J.X., L.L., and Y.C. conceived and designed the experiments. J.X. and L.L. performed the experiments. Y.G. carried out the AFM

characterization. Y.L. and R.Z. conducted the TEM characterization. F.S. performed the FIB test. J.X. and Y.C. co-wrote the paper. All authors discussed the results and commented on the manuscript. **Competing interests:** Y.C., J.X., and L.L. are inventors on a U.S. provisional patent application related to this work filed by the Board of Trustees of the Leland Stanford Junior University (application no. 62/524,197; filed 23 June 2017). All other authors declare that they have no competing interests. **Data and materials availability:** All data needed to evaluate the conclusions in the paper are present in the paper and/or the Supplementary Materials. Additional data related to this paper may be requested from the authors.

Submitted 8 July 2017

Accepted 27 October 2017

Published 29 November 2017

10.1126/sciadv.aao3170

Citation: J. Xie, L. Liao, Y. Gong, Y. Li, F. Shi, A. Pei, J. Sun, R. Zhang, B. Kong, R. Subbaraman, J. Christensen, Y. Cui, Stitching h-BN by atomic layer deposition of LiF as a stable interface for lithium metal anode. *Sci. Adv.* **3**, eaao3170 (2017).

Stitching h-BN by atomic layer deposition of LiF as a stable interface for lithium metal anode

Jin Xie, Lei Liao, Yongji Gong, Yanbin Li, Feifei Shi, Allen Pei, Jie Sun, Rufan Zhang, Biao Kong, Ram Subbaraman, Jake Christensen and Yi Cui

Sci Adv 3 (11), eaao3170.
DOI: 10.1126/sciadv.aao3170

ARTICLE TOOLS

<http://advances.sciencemag.org/content/3/11/eaao3170>

SUPPLEMENTARY MATERIALS

<http://advances.sciencemag.org/content/suppl/2017/11/27/3.11.eaao3170.DC1>

REFERENCES

This article cites 55 articles, 3 of which you can access for free
<http://advances.sciencemag.org/content/3/11/eaao3170#BIBL>

PERMISSIONS

<http://www.sciencemag.org/help/reprints-and-permissions>

Use of this article is subject to the [Terms of Service](#)

Science Advances (ISSN 2375-2548) is published by the American Association for the Advancement of Science, 1200 New York Avenue NW, Washington, DC 20005. 2017 © The Authors, some rights reserved; exclusive licensee American Association for the Advancement of Science. No claim to original U.S. Government Works. The title *Science Advances* is a registered trademark of AAAS.